Journal of The Electrochemical Society, **163** (14) A3131-A3139 (2016)
0013-4651/2016/163(14)/A3131/9/$33.00 © The Electrochemical Society

Mechanical-Electrochemical Modeling of Agglomerate Particles in Lithium-Ion Battery Electrodes

Bin Wu and Wei Lu[z]

Department of Mechanical Engineering, University of Michigan, Ann Arbor, Michigan 48109, USA

Many electrode materials for lithium-ion battery applications are composed of secondary particles. Such an active material particle is not a solid particle, but consists of many fine primary particles. This work presents a coupled mechanical and electrochemical model to predict the intercalation-induced stress in a secondary particle with an agglomerate structure. In this model the electrochemical and transport processes are accounted for at both the secondary and primary particle levels. For mechanical analysis the secondary particle is treated as a continuum with stress calculated through lithium concentration and elastic deformation. With this model we revealed several important factors that affect stresses in secondary particles. Our simulations show that a stronger dependence of the open circuit potential of the active material on lithium-ion concentration reduces the stress level. A larger magnitude of over-potential at the surface of a secondary particle causes larger stresses. A larger primary particle size helps to reduce the stresses in the secondary particle as long as the secondary particle is a continuum containing many primary particles. Finally, a comparison between a porous secondary particle and a solid particle of the same size shows that the stress level in a porous secondary particle is much smaller.

Manuscript submitted September 20, 2016; revised manuscript received October 25, 2016. Published November 29, 2016.

Lithium-ion batteries are widely used in applications ranging from cell phones, laptop computers to electric vehicles. Being able to provide a long cycle life is key to the lithium-ion battery technology. Mechanical degradation is one of the most significant mechanisms that affect the cycle life.[1] At the particle level, researchers have observed the formation of cracks and fractures in both cathode and anode active material particles, such as $LiCoO_2$ (LCO),[2] $LiNi_{0.8}Co_{0.15}Al_{0.05}O_2$ (NCA)[3] and graphite.[4] The cracks and fractures lead to isolation of active materials, disruption of the electrically conductive particle network and exposure of fresh surfaces that cause side reactions. These effects significantly reduce the battery capacity and increase the internal resistance. At the electrode level, X-ray computed tomography has shown evident deformation of the wounded electrode in cycled batteries.[5] The deformation increases the distance between anode and cathode, resulting in a loss of contact between the active materials and current collectors. This effect leads to an increase in electrical resistance and degradation of capacity.

Modeling and simulation are essential approaches to study the generation and effects of stress inside batteries. For instance, the volume change and stress of a spherical particle during lithium-ion intercalation has been calculated.[6] Treating the intercalation-induced stress analogously to thermal stress, a coupled mechanical and electrochemical model has been developed to study the stress and concentration inside a particle.[7] This particle level model has been widely used and extended to study various problems at both particle and cell levels, such as to calculate the thickness change of a pouch cell during discharge,[8] to study the stress generation in a LMO and NCA blended electrode,[9] and to study stress generation when both intercalation and phase transition happens simultaneously in a particle.[10] Nevertheless, it should be noted that these models are based on the assumption of solid particles. This assumption does not apply for active materials with an agglomerate structure, such as NCA.[3] In these materials, many nanometer-scale primary particles agglomerate to a micrometer-scale secondary particle by the adhesion of binder. The secondary particle is porous rather than a compact solid, as the electrolyte is found to be soaked into the agglomerate.[3] Therefore, charge transfer reactions are expected to occur between the primary particle surface and the electrolyte inside a secondary particle. Active materials composed of secondary particles are becoming more common for new battery materials.

To investigate the characteristic of an agglomerate, researchers have proposed several electrochemical models to account for the effects of its internal structure. The agglomerate of $LiFePO_4$ crystals has been investigated to estimate active material utilization.[11] An electrochemical impedance model has been proposed for a secondary particle.[12] A time-domain model considering particles as agglomerates has been developed.[13] While these efforts have offered important insights into the agglomerate structure and its impact on electrochemical processes, no mechanical model has been developed to study the stress in agglomerates for lithium-ion batteries. Meanwhile, multiple experiments have reported observations of fracture of agglomerates after cycling,[3] which is a major mechanism of capacity degradation. This calls for a fully understanding of the mechanical behaviors at the agglomerate level.

The objective of this work is to develop an electrochemical and mechanical coupled model for a secondary particle. Instead of considering it as a solid particle, we modelled a porous secondary particle by including the effects of electrochemical reactions inside the agglomerate. Our simulation results revealed that a major concentration gradient exists along the radius of the secondary particle, while the concentration is fairly uniform in each primary particle. Using the effective mechanical properties of the agglomerate, we incorporated mechanics equations into the model to capture the stress generation in the secondary particle. We identified several key factors that affect the stress level, including the primary particle size and the open circuit potential (OCP) profile. We also compared the mechanical behaviors of a porous secondary particle and a solid particle of the same size. The vast difference highlighted the importance of having a coupled electrochemical and mechanical porous model for a secondary particle.

Model Development

In our model the electrochemical part is built-up by applying the porous electrode theory at the secondary particle level.[13] We further extended the approach and incorporated the diffusion equation for primary particles to capture the holistic concentration distribution in both secondary and primary particles. The mechanical part is incorporated by integrating the concentration distribution and mechanical equations to obtain the intercalation-induced stress and displacement.

Electrochemical model.—A secondary particle consists of fine primary particles, binders and pore space between the solids. The pore space is assumed to be filled with electrolyte. This assumption leads to the introduction of equations describing the concentration and potential distributions of electrolyte into the model.

Figure 1a shows the schematic of the model, where R represents the coordinate along the radius of a secondary particle and r represents the coordinate along the radius of a primary particle.

Assumptions used in the model are listed below:

[z]E-mail: weilu@umich.edu

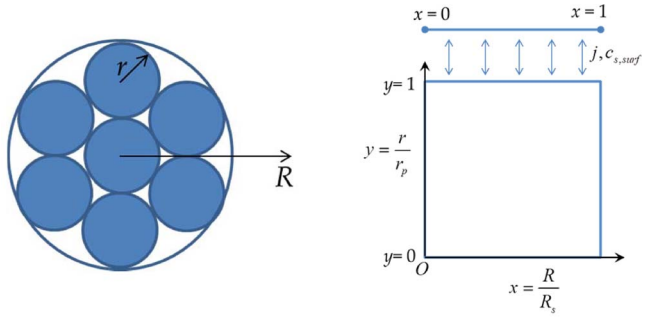

(a) Agglomerate structure (not to scale) (b) Dimensionless model

Figure 1. Schematic of the agglomerate structure and the dimensionless model.

1. The secondary particle is entirely soaked in the electrolyte. The electrolyte concentration at the surface of the secondary particle is given as the boundary condition.
2. The size of the primary particle is much smaller than that of the secondary particle, so that the secondary particle can be treated as the superposition of two continua: the electrolyte solution and solid primary particles. This treatment follows the basic assumption of the Newman's model,[14,15] which is widely used for porous electrodes.
3. Primary particles are assumed to be held together by binder rather than to be sintered together.[12,16] Since lithium ions cannot diffuse across the binder, diffusion would not occur directly between two primary particles through their contacts. Diffusion can occur between two primary particles via the electrolyte.

Following the porous electrode theory, for a spherical secondary particle the electric potential in the electrolyte phase can be expressed by

$$\frac{1}{R^2}\frac{\partial}{\partial R}\left(-R^2\kappa_l\frac{\partial\Phi_l}{\partial R}+R^2\frac{2R_gT\kappa_l}{F}(1-t_+)\frac{\partial(\ln c_l)}{\partial R}\right)=aj. \quad [1]$$

where R is the secondary particle coordinate, κ_l is the effective electrolyte conductivity, Φ_l is the electric potential in the electrolyte, R_g is the ideal gas constant, T is the absolute temperature, F is the Faraday constant, t_+ is the transference number, c_l is the electrolyte concentration, a is the active surface area per volume of the secondary particle and j is the charge transfer current density between the solid phase and the electrolyte phase. Note that $j > 0$ is for lithium ion deintercalating from the solid and $j < 0$ is for lithium ion intercalating into the solid.

The electric potential in the solid phase is given by

$$\frac{1}{R^2}\frac{\partial}{\partial R}\left(R^2\sigma_s\frac{\partial\Phi_s}{\partial R}\right)=aj, \quad [2]$$

where σ_s is the solid phase conductivity and Φ_s is the electric potential in the solid phase.

The lithium concentration in the electrolyte follows

$$\varepsilon\frac{\partial c_l}{\partial t}=\frac{1}{R^2}\frac{\partial}{\partial R}\left(R^2D_l\frac{\partial c_l}{\partial R}\right)+\frac{aj}{F}(1-t_+), \quad [3]$$

where ε is the porosity of the secondary particle and D_l is the effective electrolyte diffusion coefficient. Equations 1–3 describe the electric potential and lithium-ion concentration at the secondary particle level.

The lithium concentration in a primary particle follows the Fick's law,

$$\frac{\partial c_s}{\partial t}=\frac{1}{r^2}\frac{\partial}{\partial r}\left(D_sr^2\frac{\partial c_s}{\partial r}\right), \quad [4]$$

where c_s is the lithium concentration in the solid phase, r is the primary particle coordinate, and D_s is the solid diffusion coefficient.

Now we introduce the over-potential,

$$\eta=\Phi_s-\Phi_l-E_{ref}, \quad [5]$$

where E_{ref} is the equilibrium potential of the active material, depending on the lithium concentration in the solid.

Combining Eqs. 1, 2 and 5, we have

$$\frac{\sigma_s\kappa_l}{\sigma_s+\kappa_l}\frac{1}{R^2}\frac{\partial}{\partial R}\left(R^2\frac{\partial\eta}{\partial R}+R^2\frac{\partial E_{ref}}{\partial R}+R^2\frac{2R_gT}{F}(1-t_+)\frac{\partial(\ln c_l)}{\partial R}\right)=aj. \quad [6]$$

The charge transfer current density is given by the Butler-Volmer equation,

$$j=i_0\left(\exp\left(\alpha_a\frac{\eta F}{R_gT}\right)-\exp\left(-\alpha_c\frac{\eta F}{R_gT}\right)\right), \quad [7]$$

where i_0 is the exchange current density, α_a is the anodic reaction rate coefficient and α_c is the cathodic reaction rate coefficient. The exchange current density is given by

$$i_0=kFc_l^{\alpha_a}(c_{s,\max}-c_s)^{\alpha_a}c_s^{\alpha_c}, \quad [8]$$

where k is the reaction constant and $c_{s,\max}$ is the maximum lithium concentration in the solid.

The active surface area per volume, a, is related to porosity by

$$a=\frac{3}{r_p}(1-\varepsilon), \quad [9]$$

where r_p is the radius of the primary particle.

Dimensionless coordinates are defined as

$$x=\frac{R}{R_s},\quad y=\frac{r}{r_p}, \quad [10]$$

where R_s is the radius of the secondary particle.

With dimensionless coordinates Eq. 3 is rewritten as

$$\varepsilon\frac{\partial c_l}{\partial t}=\frac{1}{x^2R_s^2}\frac{\partial}{\partial x}\left(D_lx^2\frac{\partial c_l}{\partial x}\right)+\frac{aj}{F}(1-t_+). \quad [11]$$

Eq. 6 is rewritten as

$$\frac{\sigma_s\kappa_l}{\sigma_s+\kappa_l}\frac{1}{R_s}\frac{\partial}{\partial x}\left(\frac{\partial\eta}{\partial x}+\frac{\partial E_{ref}}{\partial x}+\frac{2R_gT}{F}(1-t_+)\frac{\partial(\ln c_l)}{\partial x}\right)=ajR_sx^2. \quad [12]$$

The gradient of the equilibrium potential is given by

$$\frac{\partial E_{ref}}{\partial x}=\frac{\partial E_{ref}}{\partial c_{s,surf}}\frac{\partial c_{s,surf}}{\partial x}=\frac{1}{c_{s,\max}}\frac{\partial E_{ref}}{\partial z}\frac{\partial c_{s,surf}}{\partial x}, \quad [13]$$

where $c_{s,surf}$ is the concentration on the surface of the primary particle and z is the stoichiometry in Li_zMO_2, such as $Li_z(Ni_{1/3}Co_{1/3}Mn_{1/3})O_2$ (NCM). The term $K = \partial E_{ref}/\partial z$, known as the thermodynamic factor in this work, represents the relationship between the equilibrium potential and the lithium concentration in the solid.

The boundary conditions for Eq. 12 are defined as

$$\begin{aligned} x=0:&\quad \frac{\partial c_l}{\partial x}=0,\ \frac{\partial\eta}{\partial x}=0\\ x=1:&\quad c_l=c_{l0},\ \eta=\eta_0, \end{aligned} \quad [14]$$

At $x = 0$, symmetric boundary conditions are used. At $x = 1$, the electrolyte concentration and over-potential are assumed to be c_{l0} and η_0. Note that both the solid and electrolyte phases on the surface of the secondary particle carry current and they can have different potentials. This is different from the typical constant current boundary condition prescribed on the solid phase in the Newman's porous electrode model, where current collectors exist at the boundary so that only the solid phase carries electric current to the current collector. Prescribing a constant current boundary condition on the surface of the secondary particle is complicated, which requires consideration of current in both the electrolyte and the solid phase. The typical constant potential condition at current collectors for constant potential operation does not apply here since the potential on the surface of the secondary

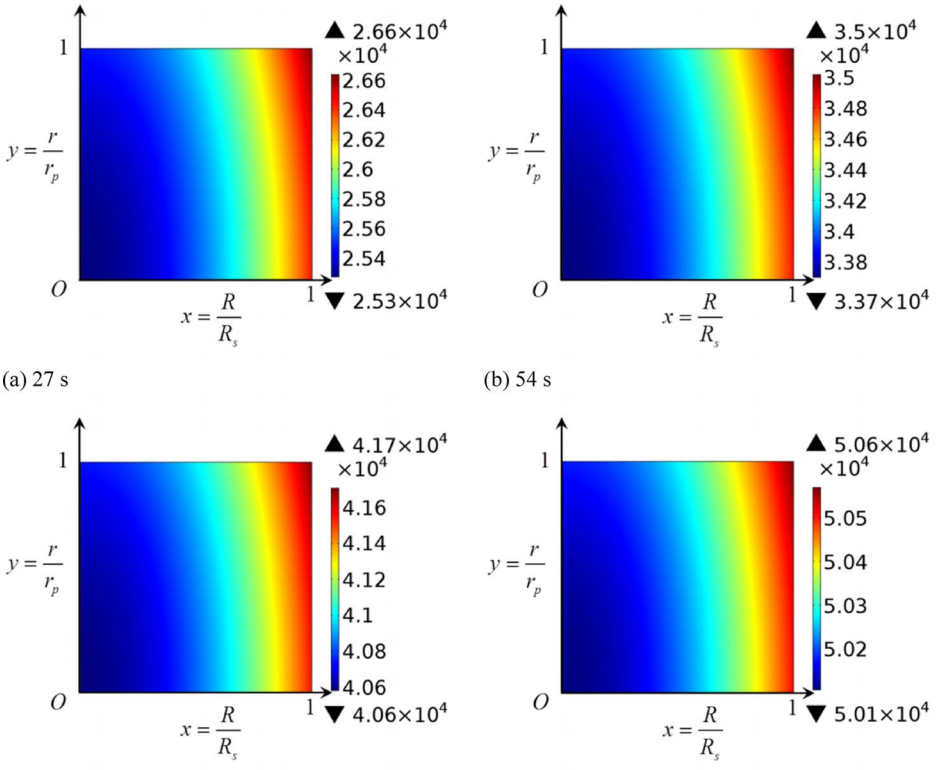

(a) 27 s (b) 54 s

(c) 82 s (d) 135 s

Figure 2. Lithium concentration distribution in primary particles at four selected times. The unit of concentration is mol/m^3. In these simulations $\eta_0 = -10$ mV and $K = -0.5$ V.

particle is not controlled. A convenient boundary condition for the secondary particle is to prescribe the over-potential on the surface, and the Dirichlet boundary conditions of c_{l0} and η_0 can be easily linked to a higher electrode-level model. In the following section, the effect of η_0 on stress generation will be investigated.

With the dimensionless coordinate, diffusion in the solid primary particle is given by

$$y^2 \frac{\partial c_s}{\partial t} = \frac{1}{r_p^2} \frac{\partial}{\partial y} \left(y^2 D_s \frac{\partial c_s}{\partial y} \right). \quad [15]$$

The boundary conditions for Eq. 15 are given by

$$\begin{aligned} y = 0: \quad & \frac{\partial c_s}{\partial y} = 0 \\ y = 1: \quad & \frac{D_s}{r_p} \frac{\partial c_s}{\partial y} = -\frac{j}{F}. \end{aligned} \quad [16]$$

Figure 1b shows the schematic of the dimensionless model. Equations at the primary particle level (Eqs. 15 and 16) and at the secondary particle level (Eqs. 7, 11, 12 and 14) are coupled through the charge transfer current density j and surface solid concentration $c_{s,surf}$. The concentration and electric potential fields are obtained by solving the coupled equations with their boundary conditions.

Figure 2 shows a representative result that gives the lithium concentration inside each primary particle along the radial direction of the secondary particle. The x axis represents the location of a primary particle inside the secondary particle, while the y axis represents the location of a spatial point inside the primary particle. As shown in Fig. 2, the primary particle shows a fairly uniform concentration. A major concentration gradient exists along the radius of the secondary particle, which is attributed to the spatial variation of the charge transfer current density to be discussed in Results and discussions section.

Mechanical model.—Simulation results from the electrochemical model revealed concentration gradient along the radius of the secondary particle. A mechanical model is developed to evaluate the stress. Assumptions used in the mechanical model are listed below:

1. The secondary particle is assumed to be mechanically homogeneous with effective properties, which can be calculated from the porosity and properties of bulk materials.
2. Because the primary particle is much smaller than the secondary particle, the secondary particle is regarded as a continuum. Each spatial point in the secondary particle is composed of many primary particles at that location. Therefore the stress at each spatial point represents the loading stress exerted on an ensemble of primary particles at that location. This loading stress is important to know since it is the cause of separation of primary particles, i.e. fracture in the secondary particle.

The effective Young's modulus, E, and Poisson's ratio, ν, of a porous microstructure can be expressed as[17]

$$\frac{E}{E_b} = \left(1 - \frac{\varepsilon}{\varepsilon_0}\right)^n, \quad \nu = \nu_0 + \left(1 - \frac{\varepsilon}{\varepsilon_1}\right)^m (\nu_b - \nu_0), \quad [17]$$

where E_b and ν_b are bulk Young's modulus and Poisson's ratio of the solid, ε_0, ε_1, n, m and ν_0 are fitted parameters obtained from the finite element simulation results of porous microstructures. The suggested values are $\varepsilon_0 = 0.652$, $n = 2.23$, $\varepsilon_1 = 0.500$,$m = 1.22$ and $\nu_0 = 0.140$ for the porous structure consisting of overlapping solid spheres.[17]

The equilibrium equation in the secondary particle is given by

$$\frac{d\sigma_r}{dR} + \frac{2}{R}(\sigma_r - \sigma_t) = 0, \quad [18]$$

where σ_r is the radial stress and σ_t is the tangential stress. The stress-strain relations are

$$\varepsilon_r = \frac{1}{E}(\sigma_r - 2\nu\sigma_t) + \frac{\Omega}{3}\tilde{c}, \quad [19]$$

Table I. Parameters used in the model.

Parameter	Symbol	Value	Reference
Primary particle radius	r_p	0.2 μm	3
Secondary particle radius	R_s	10 μm	3
Porosity of the secondary particle	ε	25%	20
Solid conductivity	σ_s	0.12 S/m	13
Solid diffusion coefficient	D_s	1×10^{-14} m^2/s	13
Electrolyte conductivity	κ_l	0.0975 S/m	13
Electrolyte diffusion coefficient	D_l	1.85×10^{-11} m^2/s	13
Initial electrolyte concentration	c_{l0}	1000 mol/m^3	13
Maximum solid concentration	$c_{s,\max}$	51830 mol/m^3	21
Initial solid concentration	c_{s0}	$0.36c_{s,\max}$	21
Reaction constant	k	6.15×10^{-11} m$^{2.5}$ mol$^{0.5}$ s^{-1}	22
Transference number	t_+	0.38	13
Temperature	T	298 K	13
Anodic reaction rate coefficient	α_a	0.5	23
Cathodic reaction rate coefficient	α_c	0.5	23
Bulk Young's modulus	E_b	100 GPa	24
Bulk Poisson's ratio	ν_b	0.24	25
Partial molar volume	Ω	3.497×10^{-6} m^3/mol	7

$$\varepsilon_t = \frac{1}{E}\left[\sigma_t - \nu(\sigma_r + \sigma_t)\right] + \frac{\Omega}{3}\tilde{c} \qquad [20]$$

where Ω is the partial molar volume of lithium ion and $\tilde{c}(R) = c_{s,surf}(R) - c_{s0}$ is the change of surface concentration of the primary particle located at position R in the secondary particle. c_{s0}, the initial lithium concentration, is defined in Table I.

Take u as the radial displacement. The strains can be expressed by

$$\varepsilon_r = \frac{du}{dR}, \quad \varepsilon_t = \frac{u}{R}. \qquad [21]$$

Eqs. 18–21 can be solved by combining them into a displacement equation 7. With the boundary condition of $\sigma_r(R = R_s) = 0$, the stress and displacement in the secondary particle are given by

$$\sigma_r = \frac{2\Omega E}{3(1-\nu)}\left(\frac{1}{R_s^3}\int_0^{R_s}\tilde{c}r^2dr - \frac{1}{R^3}\int_0^{R}\tilde{c}r^2dr\right), \qquad [22]$$

$$\sigma_t = \frac{\Omega E}{3(1-\nu)}\left(\frac{2}{R_s^3}\int_0^{R_s}\tilde{c}r^2dr + \frac{1}{R^3}\int_0^{R}\tilde{c}r^2dr - \tilde{c}\right), \qquad [23]$$

$$u = \frac{R\Omega}{3}\left[\frac{2(1-2\nu)}{(1-\nu)}\frac{1}{R_s^3}\int_0^{R_s}\tilde{c}r^2dr + \frac{(1+\nu)}{(1-\nu)}\frac{1}{R^3}\int_0^{R}\tilde{c}r^2dr\right]. \qquad [24]$$

In Eqs. 22 and 23 tensile stress is positive while compressive stress is negative.

Special attention should be given at $R = 0$ for Eqs. 22–24 as they include the term $\frac{1}{R^3}\int_0^R \tilde{c}r^2dr$, where R appears in the denominator. We shall use L'Hôpital's rule at $R = 0$, which gives

$$\lim_{R\to 0}\frac{1}{R^3}\int_0^R \tilde{c}r^2dr = \frac{\tilde{c}(R=0)}{3}. \qquad [25]$$

The calculated stress in the secondary particle can be comparted to the continuum material properties of the secondary particle to determine fracturing which is related to separation between primary particles, or yielding which is related to sliding between primary particles. It should be noted that stress concentration occurs at the contact points between primary particles,[18] while our model gives the homogenized stress at any spatial point. To capture the local contact stress between primary particles, one can explicitly model an ensemble of primary particles and their geometries using finite element, and apply the stress calculated from Eqs. 22 and 23 as the boundary conditions of the ensemble. This bridging of scales allows analyzing various local mechanical behaviors between primary particles.

Parameters.—Table I lists the parameters used in the model, which are applicable to an agglomerate of NCM. The mechanical properties of NCM are rarely given in the literature, so the values of LMO are used which are in the similar range.

Two concentration dependent parameters, κ_l and D_l, are assumed as constant for simplicity. This assumption is acceptable considering the small scale of agglomerate and therefore small variation in electrolyte lithium concentration. In addition, κ_l and D_l listed in Table I are calculated from the intrinsic values of electrolyte and porosity of the secondary particle using the Bruggeman correlation, where the tortuosity τ is assumed as $\varepsilon^{-0.5}$.

Although the electrical conductivity of the electrode can be found in the literature,[19] the conductivity of the agglomerate itself is still not clear. As the conductive additive mainly enhances the electrical conductivity at the electrode level rather than at the agglomerate level, it has been suggested that the electrical conductivity of the NCM agglomerate accounts for only 0.1% of that of the cathode.[13] We adopted this suggested value of electrical conductivity for the agglomerate.

The model was implemented using the finite element software package COMSOL Multiphysics.

Results and Discussion

Figures 3a and 3b show the radial and tangential stresses in the secondary particle at five selected times. With the intercalation of lithium ions, the expansion of the particle results in tensile radial stress. Due to the strain differential between the outer and inner regions of the particle, the tangential stress is compressive at the surface while tensile at the center. As indicated in Eqs. 22 and 23, a larger concentration gradient in the secondary particle leads to a large stress. In Figs. 3a and 3b, both stresses increase during the period of 0 s to 27 s and then decrease, suggesting that the concentration gradient reaches its maximum at around 27 s. This is supported by the concentration distribution shown in Fig. 2.

As lithium ions cannot diffuse directly across primary particles, the current density at the primary particle surface is the predominant factor that determines the concentration inside the primary particle. Hence, the lithium concentration gradient in the solid phase of the secondary particle stems from the variation in surface current density

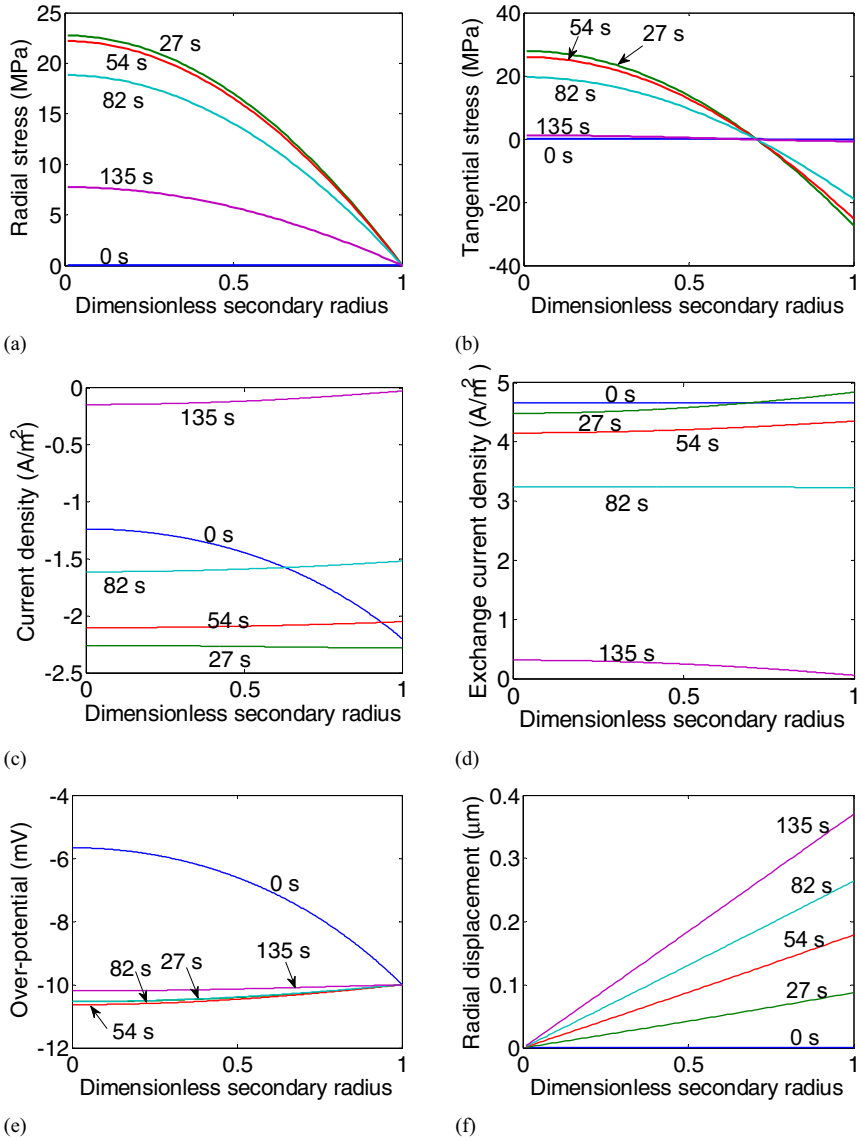

Figure 3. Stress, current density, over-potential and radial displacement along the radius of the secondary particle at five selected time. (a) Radial stress. (b) Tangential stress. (c) Current density. (d) Exchange current density. (e) Over-potential. (f) Radial displacement. For all these simulation results, $\eta_0 = -10\,\text{mV}$ and $K = -0.5\,\text{V}$.

of primary particles. Figure 3c shows that the originally non-uniform current density becomes uniform after 27 s, which is consistent with the evolution of concentration gradient. Another note taken from Fig. 3c is that the rate of lithium intercalation, $|j|$, decreases after 27 s. Therefore, the concentration gradient inside a primary particle built up before 27 s has an opportunity to be gradually smoothened. The shape of current density curves can be explained by the exchange current density and the over-potential, as shown in Figs. 3d and 3e.

The exchange current density at the surface of the secondary particle is slightly larger than that at the center in the beginning, because the electrolyte concentration keeps constant at the surface while the lithium ions in electrolyte is consumed at the center of the secondary particle. As the primary particles at the outer region gradually become saturated with intercalated lithium ions, the exchange current at the center slightly surpasses the exchange current at the surface after 82 s. In addition, Fig. 3d shows that the exchange current density pronouncedly decreases with time, as the primary particles are gradually intercalated to full. This trend explains the decrease in the intercalation rate $|j|$, as shown in Fig. 3c.

Initially, the spatial variation of exchange current is much smaller than that of current density, implying that over-potential plays a significant role in determining the distribution of current density. Figure 3e shows that the distribution of over-potential is non-uniform at 0 s but approaches uniform at later times. The transition of over-potential distribution can be elaborated through two negative feedback mechanisms. Note that the over-potential is fixed at the surface of the secondary particle.

In the first mechanism, a decrease of η (meaning an increase of $|\eta|$ since $\eta < 0$) leads to an increase of the lithium intercalation rate $|j|$, which further results in a faster increase of c_s and thus a faster decrease of E_{ref}. As E_{ref} is always positive and appears as an additive term next to η in Eq. 12, the faster decrease of E_{ref} finally leads to an increase of η. We regard this negative feedback as the thermodynamic feedback due to the role played by E_{ref}. A strong dependence of E_{ref} on c_s causes significant contribution of the thermodynamic feedback, which will be discussed in the following section.

In the second mechanism, a decrease of η results in a faster increase of c_s, consequently leading to a decrease of i_0 and $|j|$. As the intercalation current is the source term in Eq. 12, the decrease of $|j|$ (meaning an increase of j since $j < 0$) finally contributes to the increase of η. We regard this negative feedback as the kinetic feedback owing to the interplay between η and $|j|$.

Figure 3f shows the radial displacement in the secondary particle at five selected times. The displacement is almost linear along the radius of the secondary particle, and the displacement at the surface is the largest. It should be noted that the maximum radial displacement is nearly 0.36 μm, which only accounts for 3.6% of the

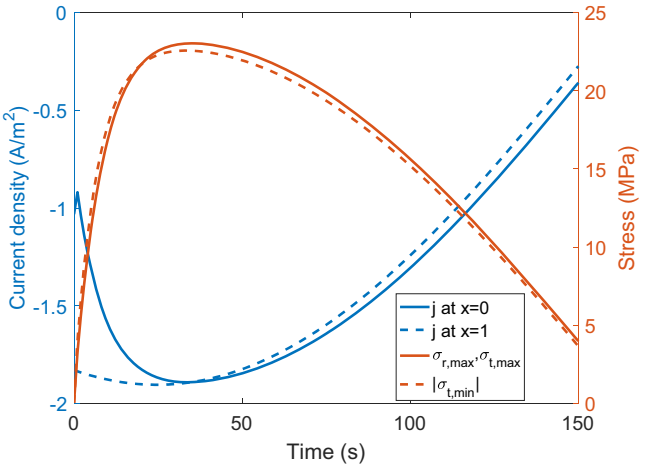

Figure 4. Maximum tensile stress, maximum compressive stress and current density with respect to time. As the compressive stress is negative, the absolute value of the compressive tangential stress is plotted. The maximum radial stress always equals to the maximum tangential tensile stress.

radius of the second particle. The calculated radial displacement at the secondary particle surface can serve as an input to an electrode-level model to calculate the electrode thickness change during discharge.

Maximum stresses are important to evaluate the mechanical integrity of the secondary particle. The maximum radial stress and the maximum tensile tangential stress are equal and are located at the center of the secondary particle,

$$\sigma_{r,\max} = \sigma_{t,\max} = \frac{2\Omega E}{3(1-\nu)}\left(\frac{1}{R_s^3}\int_0^{R_s}\tilde{c}r^2dr - \frac{\tilde{c}(R=0)}{3}\right). \quad [26]$$

The maximum compressive tangential stress is located at the surface,

$$\sigma_{t,\min} = \frac{\Omega E}{3(1-\nu)}\left(\frac{3}{R_s^3}\int_0^{R_s}\tilde{c}r^2dr - \tilde{c}(R=R_s)\right), \quad [27]$$

where the subscript "min" is used since the compressive stress is negative.

Figure 4 shows that the peaks of $\sigma_{r,\max}$, $\sigma_{t,\max}$ and $|\sigma_{t,\min}|$ are reached at around 27 s, a time when the spatial distribution of current density along the secondary particle radius becomes uniform. Literature has shown that in a solid particle $|\sigma_{t,\min}|$ should be greater than $\sigma_{r,\max}$ and $\sigma_{t,\max}$ under a constant rate of lithium ion intercalation.[9] In contrast, the results in Fig. 4 show that $|\sigma_{t,\min}|$ is not always larger than $\sigma_{r,\max}$ and $\sigma_{t,\max}$ for a porous secondary particle. This difference in the characteristics of maximum stress can be explained by the differences in governing equations and boundary conditions. Previous literature is based on the governing equation of diffusion in a solid particle with a constant Neamann boundary condition at the surface.[9] This work modeled the electrolyte phase in a porous secondary particle and adopted the Dirichlet boundary condition at the surface of the secondary particle.

Thermodynamic factor.—In this section we examine the effect of thermodynamic factor K on the stress generation behavior. The thermodynamic factor is defined as the dependence of OCP on the stoichiometry of the active material in Electrochemical model section. Figure 5 shows the stress and concentration distributions for K = -1 V and $K = 0$ V at the instant when the maximum radial stress peaks. A larger magnitude of K represents a stronger effect of the thermodynamic feedback mechanism, leading to more uniform concentration distribution and smaller stresses. This is supported by the comparison of the two cases shown in Fig. 5.

Figure 6 shows the distribution of current density and over-potential for $K = 0$ V at the same selected times as those in Fig. 3. As $K = 0$ V represents the special case of no thermodynamic negative feedback, both the current density and over-potential show large variation along the radius of the second particle at 135 s. The large spatial variation in current density directly results in a large

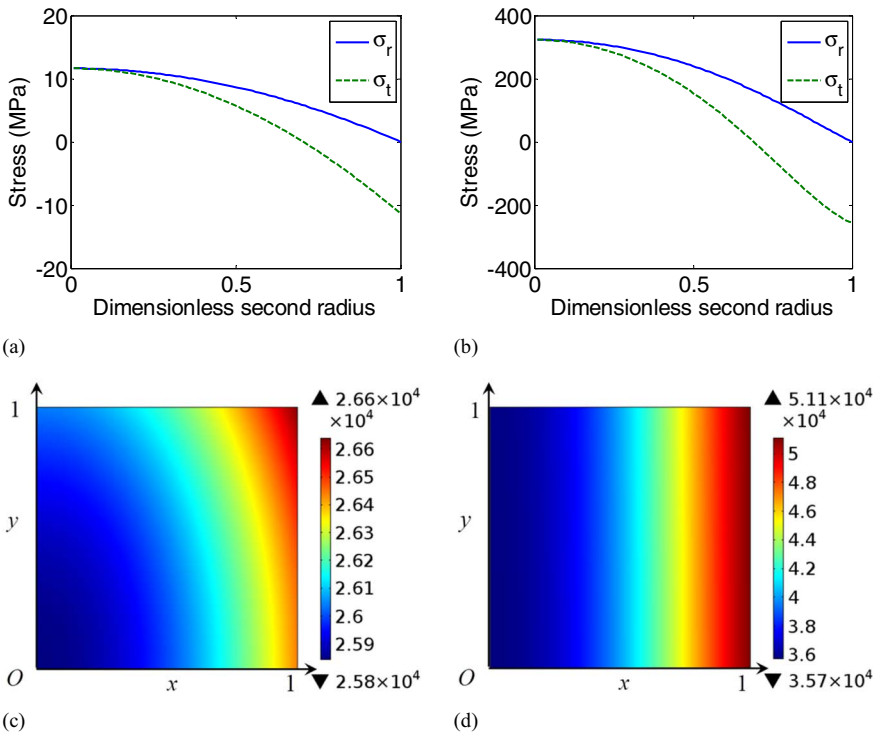

Figure 5. Stress and concentration distributions for different thermodynamic factors. For (a) and (c), $K = -1$ V. For (b) and (d), $K = 0$ V. The presented time is at the instant when the radial stress at the center reaches its maximum. The unit of concentration is mol/m^3 in (c) and (d).

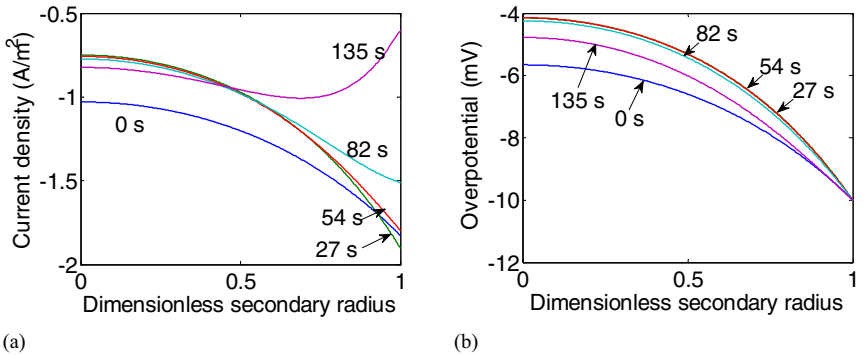

Figure 6. The distribution of (a) current density and (b) over-potential at five selected times. For the simulation results, $\eta_0 = -10\,\text{mV}$ and $K = 0\text{V}$.

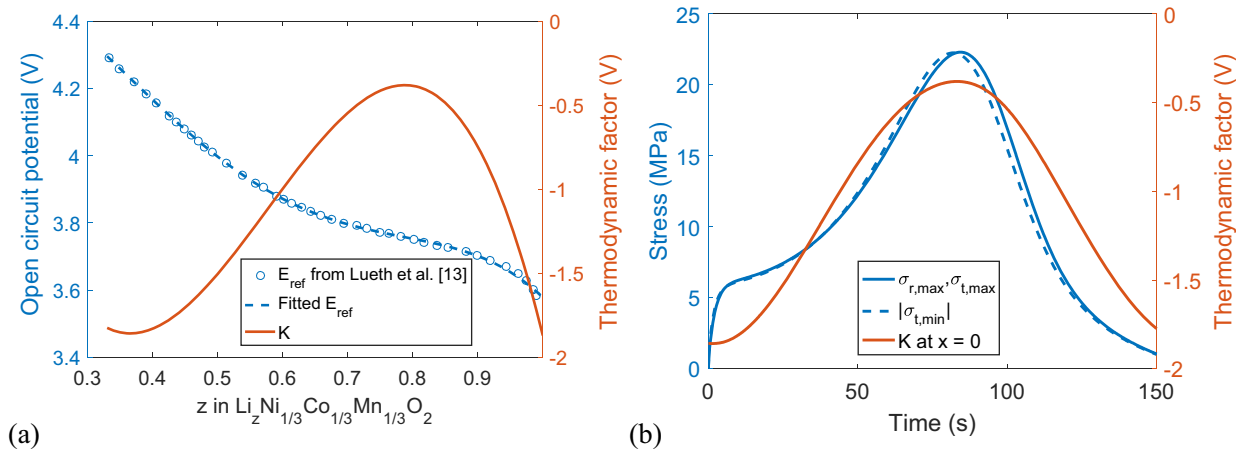

Figure 7. (a) Open circuit potential (E_{ref}) and thermodynamic factor (K) with respect to the stoichiometry in $\text{Li}_z(\text{Ni}_{1/3}\text{Co}_{1/3}\text{Mn}_{1/3})\text{O}_2$. (b) Simulated stress using the open circuit potential profile in (a). For the simulation results, $\eta_0 = -10\,\text{mV}$.

concentration gradient along the radius of the secondary particle, as shown in Fig. 5d. The magnitude of current density at the center surpasses the current density at the surface at 135 s, which is a result of heavy depletion of available lithium intercalation sites at the surface during 0∼82 s. The reverse in the current density distribution is ascribed to the kinetic negative feedback. However, this reverse occurs near the end of discharge, leaving a still large concentration gradient.

The value of K can be determined from the OCP-z profile, which is shown in Fig. 7a. Figure 7b illustrates the temporal evolution of $\sigma_{r,\max}$, $\sigma_{t,\max}$ and $|\sigma_{t,\min}|$ using the OCP-z profile shown in Fig. 7a. Previous discussions have concluded that small magnitude of K results in non-uniform current density and thus large stresses. This is further shown in Fig. 7b, where the stresses and the thermodynamic factor demonstrate similar trends with respect to time. The different values of K at different regimes of state of charge result in a change of stress in the course of intercalation or deintercalation, which may result in fatigue and reduced strength of the secondary particle.

Over-potential.—The electrochemical model uses a given over-potential η_0 at the surface of the secondary particle. This treatment can be easily linked to an electrode-level model, where the over-potential at any spatial point across the electrode thickness can be calculated and coupled to the particle level model. Figure 8 shows that the maximum radial stress increases almost linearly with the magnitude of η_0. A larger $|\eta_0|$ not only causes a larger intercalation rate $|j|$, but also a non-uniform distribution of intercalation rate along the radius of the secondary particle. It is this non-uniform intercalation rate that results significant stress, as discussed previously.

Previous studies have investigated the maximum radial stress for a solid particle under different discharge rates.[6,7] These results showed that the maximum radial stress firstly increases but then decreases with the current density. The latter decrease in stress results from the fact that the concentration gradient is still undeveloped at the end of discharge under a large discharge current. In contrast, Figure 8 shows only an increase of the maximum stress with the magnitude of over-potential, which is positively correlated with the current density. This feature comes from the characteristic of the porous secondary particle model. The distribution of current density determines the concentration gradient along the radius of the secondary particle. The current density gradient is established immediately at the beginning of discharge, as there is no time-derivative term in Eq. 12. Hence, a large concentration gradient can still develop before the end of discharge even when a large magnitude of over-potential is used as the boundary condition.

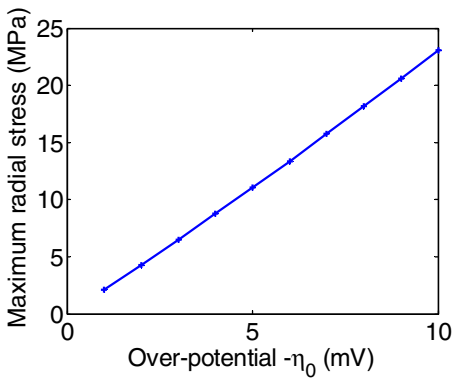

Figure 8. Maximum radial stress increases with the magnitude of over-potential.

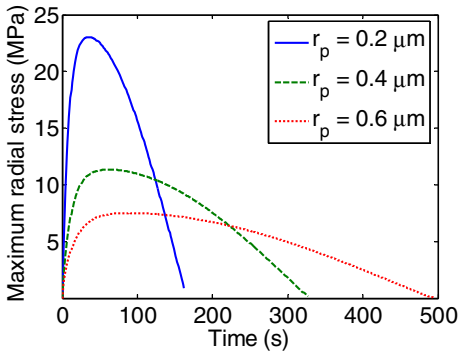

Figure 9. Maximum radial stress as a function of time for three different primary particle radii (r_p).

Primary particle size.—Figure 9 shows the effect of primary particle size on the maximum radial stress during intercalation. Interestingly, a smaller primary particle size leads to a larger maximum radial stress. This is understandable when considering the role of the active surface area per volume. As defined in Eq. 9, the active surface area per volume decreases with the radius of the primary particle. This variable appears before the current density j as the source term in Eq. 6. A large active surface area per volume amplifies the spatial variation in current density, leading to larger concentration gradient and stress. Thus, the peak of maximum radial stress decreases with the increase of the primary particle size.

Figure 10 compares the current density at the center ($x = 0$) and at the surface ($x = 1$) of the secondary particle with different size of primary particles. The current density difference between the center and the surface in Fig. 10a is larger than that in Fig. 10b, demonstrating the effect of the active surface area per volume.

The effect of diffusion inside the primary particle becomes more important with the increase of the primary particle size. Figure 11 demonstrates the concentration distribution of the agglomerate at the time when the maximum radial stress reaches its peak. With larger primary particle sizes, the concentrations in the primary particles become more non-uniform. This concentration gradient in a primary particle can induce an additional stress inside the primary particle. It should be noted that this additional stress has little effect on the interaction between particles since it is internal, while the calculated stress at the secondary particle level affects the interaction between primary particles significantly. Fracture often happens between primary particles due to their weak bonding. The stress at the secondary particle level is important in determining the fracture of an agglomerate.

Comparison with a solid particle of the same size.—The stresses in a porous secondary particle and in a solid particle of the same size are compared in Fig. 12. The stress in a solid particle is much larger than that in a porous secondary particle, which can be attributed to two reasons. First, the Young's modulus of the solid particle (100 GPa) is nearly three times as large as that of a porous secondary particle (34 GPa). As shown in Eqs. 22 and 23, the stress is proportional to the Young's modulus, leading to three times larger stress in the solid particle. Second, and more importantly, the concentration gradient in the porous secondary particle is much smaller than that in the solid particle. The electrolyte inside the porous secondary particle provides a fast diffusion path for lithium ions, which greatly reduces the concentration gradient. Note that the current density at the surface of the solid particle shown in Fig. 13 is close to the current density at the surface of the primary particle surface shown in Fig. 3c, suggesting that the pronounced difference in stress is not from the difference in current density.

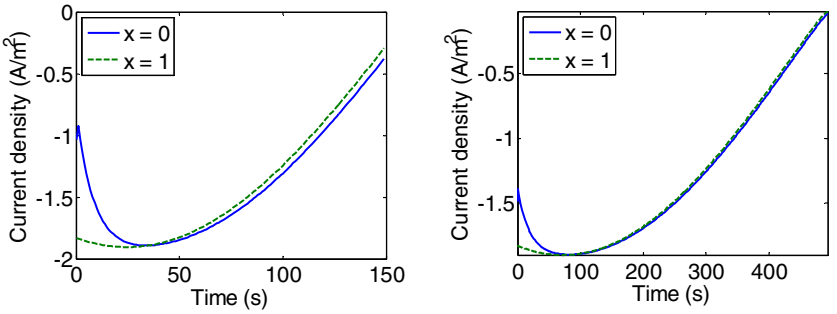

(a) $r_p = 0.2$ μm (b) $r_p = 0.6$ μm

Figure 10. Current density evolution at the center ($x = 0$) and surface ($x = 1$) of the secondary particle for (a) $r_p = 0.2\,\mu$m and (b) $r_p = 0.6\,\mu$m.

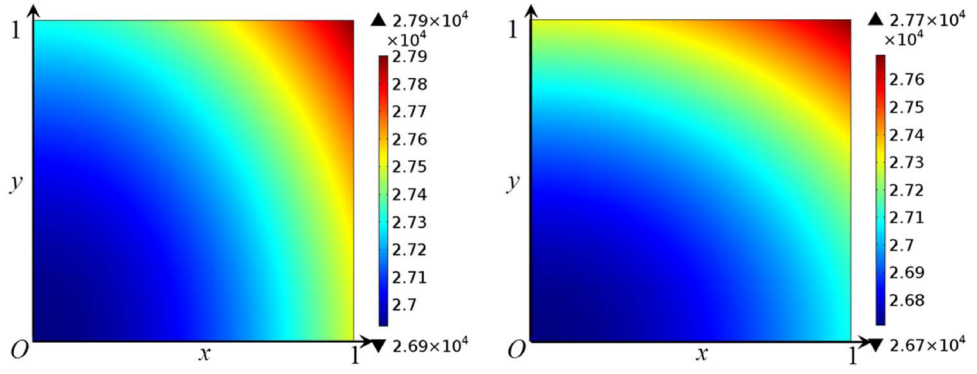

(a) $r_p = 0.4$ μm (b) $r_p = 0.6$ μm

Figure 11. Concentration distribution at the time when maximum radial stress reaches its peak for (a) $r_p = 0.4\,\mu$m and (b) $r_p = 0.6\,\mu$m. The unit of concentration is mol/m^3.

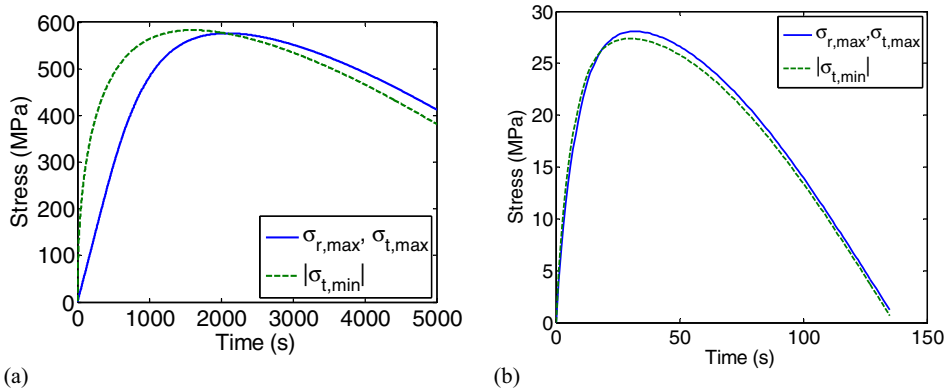

Figure 12. Maximum stresses of (a) a solid particle and (b) a porous secondary particle. For these simulation results, $\eta_0 = -10\,\text{mV}$.

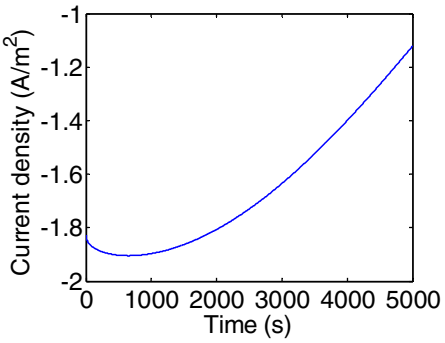

Figure 13. Current density at the surface of the solid particle.

Conclusions

In this work, an electrochemical and mechanical coupled model is developed to calculate the stress generation in a secondary particle consisting of many primary particles. As the electrolyte fills the pore between primary particles, charge transfer reactions are assumed to take place inside the secondary particle, leading to the introduction of governing equations for electrolyte concentration and electrolyte potential. Simulation results reveal that a major concentration gradient exists along the radius of the secondary particle, while the concentration distribution in each primary particle is fairly uniform. Based on this finding, the mechanical model focused on the stress generation at the secondary particle level. Assuming the secondary particle a continuum, the intercalation-induced stress is calculated using elastic equations.

We have applied the developed model to investigate factors affecting the stress generation behaviors. The results are summarized as follows under the condition that the size of the primary particle is much smaller than that of the secondary particle so that the continuum approach applies: 1) A strong dependence of OCP on the solid lithium concentration leads to a more uniform current density in the secondary particle, which reduces the stress level. 2) A large magnitude of over-potential at the secondary particle surface causes severely non-uniform current density, and thus larger stresses. 3) The primary particle size shows a significant effect on the current density, concentration and stress profiles. A larger primary particle size results in a smaller active surface area per volume, which reduces the impact of non-uniform current density and thus reduces the stress level in the secondary particle. However, the concentration gradient inside the primary particle becomes pronounced with the increase of the primary particle size, which may generate stress inside the primary particle. 4) The comparison between a porous secondary particle and a solid particle of the same size shows that the stress is greatly alleviated in the porous secondary particle. This is attributed to the lower Young's modulus of the porous particle, and more importantly, to the smaller concentration gradient in the porous secondary particle.

In this work we treat the secondary particle as a continuum in the stress calculation. In practical applications, the continuum approach is generally applicable since the size of the primary particle is often only a few percent or less of that of the secondary particle. The stress at each spatial point represents the loading stress exerted on the primary particles at that location. This loading stress can lead to fracture in the secondary particle in terms of separation of primary particles. We plan to study this fracture behavior in future work by applying the stress predicted by this model as the loading boundary conditions on a representative volume of the particle network. In addition, the model proposed in this work can be incorporated into a cell level mechanical model to provide valuable insights into the overall battery degradation.

Acknowledgment

This work was supported by the National Science Foundation under grant No. CNS-1446117.

References

1. J. Christensen, *J Electrochem Soc*, **157**, A366 (2010).
2. H. Wang, Y.-i. Jang, B. Huang, D. R. Sadoway, and Y.-m. Chiang, *J Electrochem Soc*, **146**, 473 (1999).
3. D. Abraham, D. Dees, J. Knuth, and E. Reynolds, *ARGONNE National Laboratory (ANL-05/21)*, 196 (2005).
4. K. Takahashi and V. Srinivasan, *J Electrochem Soc*, **162**, A635 (2015).
5. T. Waldmann, S. Gorse, T. Samtleben, G. Schneider, V. Knoblauch, and M. Wohlfahrt-Mehrens, *J Electrochem Soc*, **161**, A1742 (2014).
6. J. Christensen and J. Newman, *J Electrochem Soc*, **153**, A1019 (2006).
7. X. Zhang, W. Shyy, and A. Marie Sastry, *J Electrochem Soc*, **154**, A910 (2007).
8. B. Rieger, S. V. Erhard, K. Rumpf, and A. Jossen, *J Electrochem Soc*, **163**, A1566 (2016).
9. Y. Dai, L. Cai, and R. E. White, *Journal of Power Sources*, **247**, 365 (2014).
10. J. Park, W. Lu, and A. M. Sastry, *J Electrochem Soc*, **158**, A201 (2011).
11. S. Dargaville and T. W. Farrell, *J Electrochem Soc*, **157**, A830 (2010).
12. J. Huang, H. Ge, Z. Li, and J. Zhang, *J Electrochem Soc*, **161**, E3202 (2014).
13. S. Lueth, U. S. Sauter, and W. G. Bessler, *J Electrochem Soc*, **163**, A210 (2016).
14. M. Doyle, *J Electrochem Soc*, **140**, 1526 (1993).
15. T. F. D. Fuller and Marc. Newman John., *J Electrochem Soc*, **141**, 1 (1994).
16. J. Huang, Z. Li, J. Zhang, S. Song, Z. Lou, and N. Wu, *J Electrochem Soc*, **162**, A585 (2015).
17. A. P. Roberts and E. J. Garboczi, *Journal of the American Ceramic Society*, **83**, 3041 (2000).
18. H. Mendoza, S. A. Roberts, V. E. Brunini, and A. M. Grillet, *Electrochimica Acta*, **190**, 1 (2016).
19. N. A. Zacharias, D. R. Nevers, C. Skelton, K. Knackstedt, D. E. Stephenson, and D. R. Wheeler, *J Electrochem Soc*, **160**, A306 (2013).
20. V. Srinivasan and J. Newman, *J Electrochem Soc*, **151**, A1517 (2004).
21. T. R. Tanim, C. D. Rahn, and C.-Y. Wang, *Journal of Dynamic Systems, Measurement, and Control*, **137**, 011005 (2014).
22. S. W. Han, *Transport and Kinetic Phenomena Linked to Power Performance of Lithium-Ion Batteries*, in, University of Michigan (2014).
23. X. K. Lin, J. Park, L. Liu, Y. Lee, A. M. Sastry, and W. Lu, *J Electrochem Soc*, **160**, A1701 (2013).
24. S. Han, J. Park, W. Lu, and A. M. Sastry, *Journal of Power Sources*, **240**, 155 (2013).
25. Y. Qi and L. G. Hector Jr., C. James and K. J. Kim, *J Electrochem Soc*, **161**, F3010 (2014).